



Oxygen vacancies-driven nonradical oxidation pathway of catalytic ozonation for efficient water decontamination

Lanlan Liang^a, Peike Cao^a, Xin Qin^a, Shuai Wu^a, Haokun Bai^a, Shuo Chen^a, Hongtao Yu^a, Yan Su^b, Xie Quan^{a,*}

^a Key Laboratory of Industrial Ecology and Environment Engineering (Ministry of Education), School of Environmental Science and Technology, Dalian University of Technology, Dalian 116024, PR China

^b Key Laboratory of Materials Modification by Laser, Ion and Electron Beams (Ministry of Education), School of Physics, Dalian University of Technology, Dalian 116024, PR China

ARTICLE INFO

Keywords:

Degradation
Organic pollutants
Nonradical pathway
Ibuprofen
Actual wastewater treatment

ABSTRACT

Developing catalysts with high efficiency and excellent interference tolerance for practical application remains a challenge in catalytic ozonation process. Herein, the surface Vo-rich catalyst was successfully prepared by lattice-doping Co into zinc ferrite spinel, which exhibited efficient mineralization of recalcitrant organic pollutants. The contaminants removal was mainly attributed to the nonradical-based oxygen species of surface atomic oxygen (*O) rather than traditional hydroxyl radical (-OH). The experiments and DFT calculation results revealed that Vo was the main active sites for adsorption of ozone and production of *O. The O-O in ozone was dissociated at Vo, triggering the formation of *O. In addition, the Vo-driven nonradical catalysis showed high resistance to the coexisting ions (200 mM Cl⁻, SO₄²⁻ and NO₃⁻) and exhibited excellent performance for actual wastewater treatment. This work provides a novel strategy to regulate the oxidation pathways in catalytic ozonation process for efficient mineralization of pollutants in complicated water matrices.

1. Introduction

Advanced oxidation processes (AOPs) are powerful techniques for efficient destruction of refractory organic pollutants in aqueous environment. Among AOPs, heterogeneous catalytic ozonation (HCO) has attracted considerable attention due to the efficient mineralization of organic contaminants, wide pH range and catalyst recyclability [1–3]. In a typical HCO process, ozone can be adsorbed and decomposed over the catalysts and converted into activated oxygen species via radical (e.g. ·OH and O₂·) or alternative nonradical pathways [4,5].

The alternative nonradical-based pathways receive wide attention in recent years because of its intrinsic advantages of long life and high resistance to the coexisting ions, which can maintain efficient catalytic performance in complicated water matrices [5,6]. Generally, the nonradical-based oxygen species in HCO mainly include surface adsorbed oxygen species (*O and *O₂) and ¹O₂ [7,8]. Among them, *O owns highest oxidative potential (2.43 V) and maintains excellent degradation efficiency in the presence of coexisting ions [7–9]. The nonradical-based oxidation pathway is an important oxidation process in HCO for the

destruction of organics. For instance, Bing et al. suggested that the *O formed on Ti-doped γ-Al₂O₃ in catalytic ozonation process achieved high mineralization towards six pharmaceuticals [10]. Similar phenomenon was observed on PdO/CeO₂ with generation of *O for efficient pollutant removal [11]. Moreover, Wang et al. found that the bicarbonate ion had negligible effect on pollutants removal through the nonradical oxidation route by N-doped carbon nanotubes [9]. Although nonradical oxidation process in HCO has been studied in several researches, the accurate design and regulation of active sites for nonradical catalysis remains challenging.

Optimization and regulation of surface structure of catalysts can be capable of regulation of active sites in catalytic process. Defect engineering is regarded as an effective strategy to modulate the electronic structure and induce active centers [12]. As is well known, oxygen vacancies (Vo) were the most common anion defects in metal compound with lattice oxygen detachment. It has been reported that Vo with excess localized electrons and coordinatively unsaturated nature can significantly promote the adsorption or dissociation of molecular oxygen [12–14]. Previous researches mainly focused on enhancement of

* Corresponding author.

E-mail address: quanxie@dlut.edu.cn (X. Quan).

<https://doi.org/10.1016/j.apcatb.2022.122321>

Received 4 October 2022; Received in revised form 14 December 2022; Accepted 20 December 2022

Available online 30 December 2022

0926-3373/© 2022 Elsevier B.V. All rights reserved.

reactive oxygen species (e.g. $\cdot\text{OH}$, O_2^- and $^1\text{O}_2$) generation with Vo in catalytic ozonation process [15–17]. However, the role of Vo in manipulation of oxidation pathway was not clear. The ozone molecules (O_3) with electrophilic property are favorable to be bonded with Vo sites [17], which may facilitate the elongating of the O–O bond in O_3 molecule with proper adsorption and consequently favor the dissociation of O_3 for selective formation of nonradical active species $^*\text{O}$. Therefore, we assume that Vo can serve as the active sites for the activation of O_3 for the generation of $^*\text{O}$. To the best of our knowledge, the accurate design and manipulation of nonradical pathway by Vo in HCO is still absent and need to be explored.

To verify our hypothesis, transition spinel ferrites with adjustable Vo were selected as the catalytic ozonation catalysts, which are chemically stable, earth-abundant, and, most importantly, structurally tunable for Vo formation. In this study, the surface Vo-rich catalysts are successfully synthesized by lattice-doping Co into zinc ferrite spinel, which exhibits efficient activity for organic pollutants mineralization during the catalytic ozonation. Experiments and DFT calculation results revealed that Vo is the main active sites for the adsorption of ozone and generation of nonradical species. The surface adsorbed $^*\text{O}$ is identified as the dominant reactive oxygen species in this catalytic ozonation system. The catalytic activity performance is evaluated with inorganic ions using ibuprofen (IBU) as the target pollutant. This work provides a new perspective on nonradical oxidation process for efficient mineralization of refractory organic contaminants in complicated water matrices.

2. Experimental section

2.1. Chemical and reagents

Ibuprofen (IBU, 99 %), levofloxacin (LVFX, 99 %), tetracycline (TC, 99 %), carbamazepine (CBZ, 99 %), 4-nitrophenol (4-NP, 99 %), 5,5-Dimethyl-1-pyrroline (DMPO), 2,2,6,6-tetramethyl-4-piperidone (TEMP) were supplied by Aladdin Reagent. Methanol (HPLC grade) and acetonitrile (HPLC grade) were provided by Merck (Darmstadt, Germany). Other chemicals and reagents were purchased from Damao chemical Co., Ltd. (Tianjin, China). All chemicals are analytical grade without further purification. Ultrapure water ($18\text{ M}\Omega\text{ cm}^{-1}$) was purified by the Milli-Q water purification system (Bedford, USA).

2.2. Catalysts preparation

The catalysts were synthesized by the sol-gel citrate and calcination method based on precious literature. Typically, 2.5 mmol Zn ($(\text{CH}_3\text{COO})_2\cdot 2\text{H}_2\text{O}$), stoichiometric amount of $\text{Fe}(\text{NO}_3)_3\cdot 9\text{H}_2\text{O}$ and Co ($(\text{CH}_3\text{COO})_2\cdot 4\text{H}_2\text{O}$) (details refer to Supporting Information, Table S1) were dissolved in 30 mL diluted nitric acid (1 M) solution with vigorous stirring. Then 15 mmol citric acid was introduced into above solution. The viscous gel was then formed with heating at $100\text{ }^\circ\text{C}$ under constant stirring for 2 h. Next, the gel was heated at $140\text{ }^\circ\text{C}$ in oven for 6 h. Thereafter, the precursor was calcined at $170\text{ }^\circ\text{C}$ for 2 h and subsequently at $600\text{ }^\circ\text{C}$ for 4 h (with a heating rate of $5\text{ }^\circ\text{C min}^{-1}$), resulting in the desired spinel oxide. The Fe: Co atomic mole ratio was determined to be 1:0, 9:1, 8:2, 7:3, 6:4. The obtained materials were labeled as ZFO, ZFC-10 %, ZFC-20 %, ZFC-30 % and ZFC-40 %, respectively. The digital images of prepared catalysts were shown in Fig. S1. In addition, the Vo was also introduced on the surface of zinc ferrite spinel with hydrogenation treatment. The sample of ZFO was passed with H_2/Ar (5 v%) gas at atmospheric pressure and kept at $420\text{ }^\circ\text{C}$ for 2 h, which was labeled as ZFO-H.

2.3. Characterization

The X-ray powder diffraction (XRD) spectrum were detected on SmartLab using $\text{Cu K}\alpha$ X-ray irradiation. The surface morphology and element distribution were characterized by field-emission scanning

electron microscopy (SEM, NOVA NanoSEM, Thermo Fisher, USA) with an energy dispersive spectrometer (EDS). The high-resolution transmission electron microscopy (HR-TEM) images were collected by TF30 (Thermo scientific, USA). Raman spectra were acquired by DXR Microscope (Thermo Fisher, USA) with $\lambda_{\text{exc}} = 532\text{ nm}$. The Brunauer-Emmett-Teller (BET) specific surface area were detected by a sorption analyzer Autosorb-IQ-C (Quantachrome, USA). The functional group was investigated by Fourier transform infrared spectroscopy (FTIR, EQUINOX55, Bruker, Germany). Analysis of the number of acid sites were obtained by pyridine-FTIR with Nicolet iS50 (Thermo Fisher, USA). The surface metallic oxidation states and element valence were analyzed by X-ray photoelectron spectroscopy (XPS, k-Alpha+, Thermo Fisher Scientific Inc, USA). The electron paramagnetic resonance (EPR) signals were detected on A200–9.5/12 spectrometer (Bruker, Germany) with TEMP and DMPO as spin-trapping agents. The temperature programmed desorption of hydrogen /ammonia /carbon dioxide (H_2 -TPR/ NH_3 -TPD) experiment were performed on CHEMBET-3000 (Quantachrome, USA). The O_2 -TPD tests were taken on CHEMBET-2920 TPR/TPD equipment (Quantachrome, USA). The surface charge of catalysts was measured with a zeta potential analyzer (ZS90, Malvern, UK).

2.4. Reaction procedures

All experiments were carried out in a semi-continuous mode 500 mL glass reactor (effective volume is 250 mL). Ozone was produced with a standard ozonizer (COM-AD-01, Anshan Anseros Environmental Protection Co., Ltd, Anshan, China) supplied with pure oxygen. Typically, the catalyst powders were suspended in IBU solution (250 mL, 20 mg/L) with continuous stirring for 40 min to achieve adsorption saturation. Ozone was then bubbled into the reactor with a 0.2 L min^{-1} flow rate. The residual ozone in the off-gas was trapped by KI solution (5 wt%). At certain reaction time intervals, 4 mL sample was collected and quenched by $\text{Na}_2\text{S}_2\text{O}_3$ (0.1 M). Then the sample was filtered through a $0.45\text{-}\mu\text{m}$ polytetrafluoroethylene membrane for analysis.

2.5. Analytical methods

The concentration of IBU was tested using high-performance liquid chromatography (HPLC, Aligent, USA). Total organic carbon (TOC) was determined on an Analytikjena TOC analyzer (multi N/C@2100, Germany). The gaseous ozone concentration was monitored by an IDESL-2000 on-line ozone concentration detector (IDEAL, USA). The dissolved metal ions were quantified by inductively coupled plasma optical emission spectrometry (ICP-OES) (OPTIMA2000, PerkinElmer, USA). IBU degradation products were determined by a liquid chromatography-tandem mass spectrometer (LC-MS, Agilent 1260/6310, USA). More details about the information for in situ Raman spectra, pyridine-FTIR and LC-MS analysis were given in Supporting Information.

3. Results and discussion

3.1. Characterization of catalysts

The crystal nature of the catalysts was identified by XRD analysis. As shown in Fig. S2, the characteristic diffraction peaks of all the catalysts were indexed to planes of zinc ferrite (JCPDS No: 77-0011, Cubic phase, $a = b = c = 3.926\text{ }\text{\AA}$). In comparison with ZFO, the tiny peaks appeared in doped-samples corresponding to the ZnO impurities, the other XRD patterns exhibited the characteristic spinel diffraction peaks, suggesting the integrity of the crystal phase with Co-doping. No redundant characteristic peaks of Fe and Co oxides appeared in catalysts, suggesting the Co might be incorporated into the lattice of ZFO. With the elevated substitution of Co, the characteristic diffraction peaks of ZFC gradually shifted to the higher angles and the strength of peaks decreased, implying that Co was successfully incorporated into the spinel lattice and the crystal phase was affected by Co substitution.

The typical morphology of catalysts was obtained by SEM and TEM. The SEM of ZFC-20 % were shown in Fig. 1(a-b). The catalysts predominantly presented the morphology of spherical agglomerate nanoparticles. The TEM image (Fig. 1c) verified that the ZFC-20 % nanocomposites consisted of small nanoparticles with the size around 50–100 nm. HRTEM images (Fig. 1(d-f)) further presented a series of clear lattice fringes of 2.573 Å, 2.975 Å and 1.488 Å, which were corresponded to the (331), (220) and (440) plane of ZFO, respectively. Additionally, the EDS presented that the Zn, Fe, Co and O elements were uniformly distributed throughout the ZFC-20 % (Fig. 1 (g-k)) and the atomic ratio of each element was close to the nominal ratio (Fig. S3).

Chemical states of the catalysts were characterized by XPS. The new peak of Co2p appeared in the survey spectra of ZFC-20 % (Fig. 2a). The Zn2p spectrum of two catalysts at 1021.6 eV and 1044.7 eV corresponded to Zn2p_{3/2} and Zn2p_{1/2} (Fig. 2b), indicating the zinc mainly existed in the form of Zn(II) [18]. In Fig. 2c, the Fe2p spectrum could be divided into three pair of peaks with different binding energy values attributed to Fe2p_{3/2}, Fe2p_{1/2} and satellite peak. The characteristic peaks of Fe2p_{3/2} at 710.9 eV and Fe2p_{1/2} at 724.6 eV suggested the appearance of divalent iron in ZFC-20 % [19]. The peak of the Fe2p_{3/2} at 712.9 eV and Fe2p_{1/2} at 726.7 eV demonstrated the formation of trivalent ion in ZFC-20 %. Compared with ZFO, the peak of Fe2p shifted to lower binding energy, suggesting the electronic environment around Fe atom changed with the introduction of Co. The spin-orbit splitting peaks of Co2p were observed in XPS spectrum of ZFC-20 %. The peaks at 780.6 eV and 795.7 eV were ascribed to Co(III) and the peaks at 782.9 eV and 796.7 eV corresponded to Co(II) [18] in Fig. 2d. The high-resolution O1s spectra of ZFO and ZFC-20 % were presented in Fig. 2e. The binding energy at 529.9 eV, 531.3 eV and 532.5 eV were attributed to the lattice oxygen with metal (O_{latt}), oxygen species adsorbed on surficial Vo (O_{ads}, e.g. -OH) and surface adsorbed water molecules (O_{surf}) [13,20]. The adsorbed oxygen species was closely associated with Vo because the dissociative molecular oxygen was adsorbed on Vo [21]. The ratio of adsorbed oxygen in ZFC-20 % was much higher than that in ZFO, indicating that Co-doping induced more Vo over the surface of ZFC-20 % [18].

The chemical structure of as-prepared catalysts was determined by the FTIR and Raman spectra presented in Fig. S4. The bending vibration peaks (Fig. S4a) located at 3442 cm⁻¹ and 1628 cm⁻¹ in all spectra were caused by H₂O and O-H stretching vibration adsorbed on the surface of the materials. For ZFO, the two sharp peaks around 546 cm⁻¹ and 435 cm⁻¹ were assigned to Fe-O and Zn-O stretching vibration [22]. The bending vibration peak of ZFC-20 % shifted to higher wavenumbers, which may be attributed to the substitution of Co ion in the ZFO lattice. The Raman peak (Fig. S4b) around 346 cm⁻¹, 496 cm⁻¹ and 649 cm⁻¹ were assigned to the F_{2g}(2), F_{2g}(3) and A_{1g}, respectively, from cubic spinel structure of ZFO [23]. The A_{1g} and F_{2g} peaks were attributed to the motion of oxygen in tetrahedral AO₄ groups and octahedral BO₆ groups [22]. Additionally, the blue shift of vibration peaks suggested that Co was successfully integrated into ZFO structure.

The N₂ adsorption-desorption isotherms of catalysts were all of type IV with hysteresis loops of type H₃, suggesting the presence of mesopores in ZFO and ZFC (Fig. S5a). As presented in Table S2, the specific surface area of catalysts decreased with the increase of Co species, which was not consistent with the catalysis performance. It suggested that the specific surface area was not the key species for improved activity. According to the magnetic curves and the magnetism hysteresis loops in Fig. S5b, the magnetism of catalysts showed the consequence of ZFC-30 % > ZFC-40 % > ZFC-20 % > ZFC-10 % > ZFO. The magnetism of ZFO was significantly enhanced with the introduction of Co, which were advantageous for the separation of the catalysts from the aqueous solution.

NH₃-TPD was carried out for evaluating the amount of acid sites on the surface of catalysts (Fig. S6a). The adsorption peak intensity of ZFC-20 % was substantially greater than that of ZFO especially when temperature was above 320 °C, indicating the strong acid sites increased with the dopant of Co. Lewis acid sites were generally considered as the adsorption site of ozone in previous reports [24,25]. The types of acid sites could be identified by pyridine adsorption combined with FTIR. Pyridine vibrational bands at different temperatures (20 °C, 150 °C and 350 °C) were presented in Fig. S6(b-d). The strong IR bonds at 1489.36 cm⁻¹, 1574.70 cm⁻¹ and 1607 cm⁻¹ corresponded to the Lewis

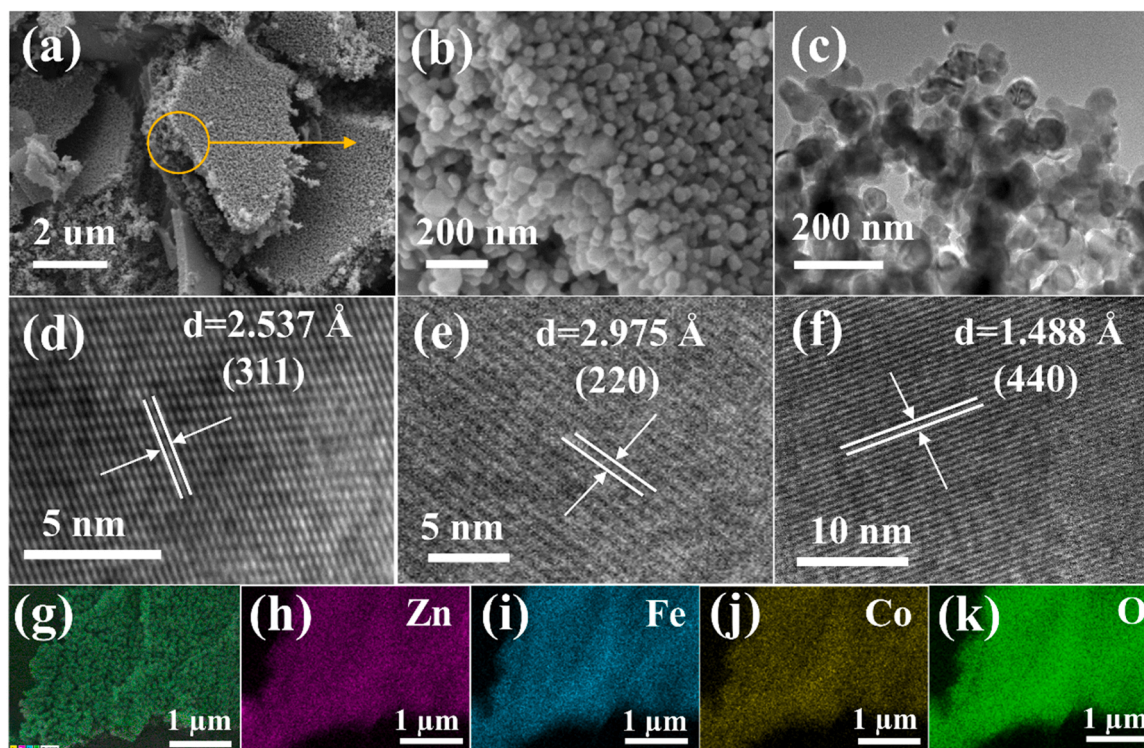


Fig. 1. (a-b) SEM, (c-f) TEM and (g-k) EDS of ZFC-20 %.

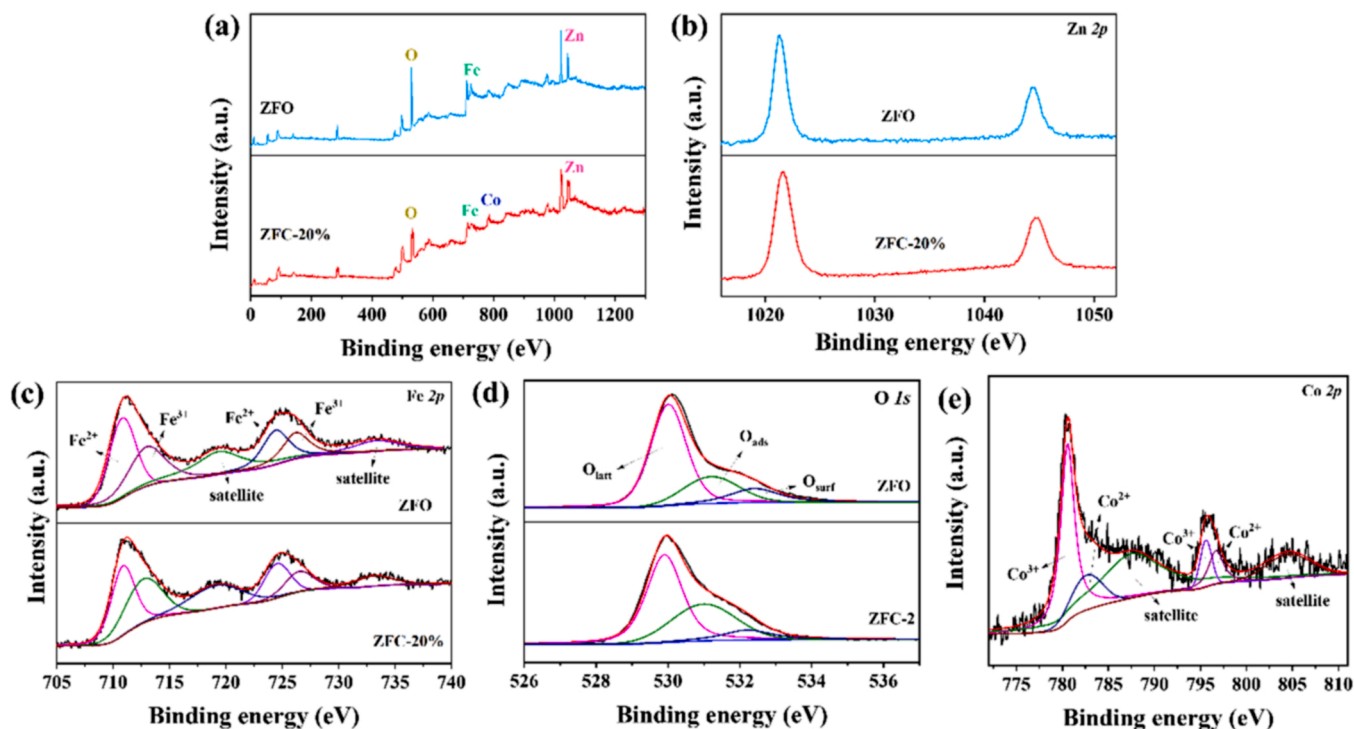


Fig. 2. (a) XPS survey scan of ZFO and ZFC-20 %, XPS high-resolution of (b) Zn 2p, (c) Fe 2p, (d) O 1s and (e) Co 2p.

acid sites on the surface of catalysts [25]. The occurrence of peak at 1489.03 cm^{-1} was attributed to the adsorption of pyridine on Lewis and Brønsted acid sites [25]. All the peak intensity of ZFC-20 % was higher than that of ZFO, suggesting that the substitution of Co in the structure of ZFO resulted in the increase of Lewis acid sites.

3.2. Catalytic activity evaluation

The catalytic activity of catalysts was evaluated using IBU as a model pollutant, which was one of the ozone-recalcitrant organic pollutants ($k_{O_3} = 9.6\text{ M}^{-1}\text{s}^{-1}$). As presented in Fig. S7a, the catalyst showed negligible IBU adsorption (<3 %). The leaching ions of $\text{Fe}^{2+}/\text{Co}^{2+}$ ($0.015\text{ mg/L Fe}^{2+}$ and $0.138\text{ mg/L Co}^{2+}$) only provided 29 % TOC removal. The sole ozonation displayed poor activity for IBU mineralization with only 21 % TOC removal within 90 min. Notably, the ZFC catalysts with the substitution of Co delivered a superior catalytic activity than ZFO or sole ozonation, suggesting Co doping favors the improvement of catalytic ozonation performance. The catalysts of ZFC with different Co ratios showed discrepant catalytic activity in IBU mineralization. Among them, catalyst of ZFC-20 % achieved the best degradation activity with 59 % TOC removal within 90 min (Fig. 3a). For kinetics investigation, the TOC removal follows pseudo-first-order kinetics (Fig. 3b). The catalyst of ZFC-20 % exhibited the highest reaction rate constant, which was 2.46-fold higher than that of ZFO. Therefore, ZFC-20 % was selected for the following experiments.

The effects of catalyst dosage, ozone concentration and initial pH on the catalytic performance were examined and presented in Fig. 3c–e. Elimination of IBU gradually improved from 40 % to 58 % within 90 min when the catalyst dosage raised from 0.02 g/L to 0.2 g/L, implying that higher ZFC-20 % dosage provided more active sites to contact with ozone for the generation of activated oxidation species. However, no obvious promotion in term of IBU mineralization was observed with further increase the catalysts concentration. Besides, mineralization efficiency of IBU was enhanced from 42 % to 61 % with the increasing ozone dosage from 15 mg/L to 35 mg/L (Fig. 3d). The effect of initial pH (4–11) on mineralization of IBU was examined in Fig. 3e. The TOC removal in ZFC-20 % catalytic ozonation was significantly enhanced

compared with sole ozonation system when pH varied from 4 to 11 (Fig. S7b). The ZFC-20 % catalyst exhibited excellent mineralization efficiency (>56 % TOC removal within 90 min) over the broad pH range of 4–9, suggesting the catalyst showed wide pH tolerance. However, the relative extreme alkaline (pH 11) conditions inhibited the contaminant abatement in ZFC-20 %/ O_3 process. The utilization efficiency of O_3 at pH 11 was similar with that at pH 4–9 (Fig. S8(a–b)), suggesting that the inhibition degradation at pH 11 was not ascribed to O_3 decomposition in ZFC-20 %/ O_3 system. Besides, the IBU adsorption decreased from 7.8 % to 3.5 % when pH increase from 4 to 11 (Fig. S8c). The reduced IBU adsorption at pH 11 was not favorable for the contact of IBU and $\cdot\text{O}$ on catalyst surface. Furthermore, the pH_{pzc} (pH at the point of zero charge) of ZFC-20 % was around 5.2 in Fig. S7c, suggesting the ZFC-20 % surface negatively charged at $\text{pH}11 > \text{pH}_{\text{pzc}}$. The pK_a value of IBU is 4.6 [26], implying that IBU in solution mainly existed in deprotonation form with negative charge at pH 11. The inhibition of catalytic activity at pH 11 might be due to the electrostatic repulsion between negative charged catalyst and IBU.

Additionally, the performance of ZFC-20 %/ O_3 system can be further evaluated by the removal of different organic pollutants, such as levofloxacin (LVFX), carbamazepine (CBZ), tetracycline (TC), 4-nitrophenol (4-NP) and oxalic acid (OA). As presented in Fig. 3f. The TOC removal for LVFX, CBZ, TC, 4-NP and OA were 63 %, 65 %, 54 %, 76 % and 56 %, respectively, suggesting that the catalytic ozonation of ZFC-20 % exhibited effective removal of refractory organic pollutions with different structures.

The stability of the catalyst was performed by five consecutive runs when the catalyst was collected by a magnet. As shown in Fig. S7d, the mineralization of IBU declined 12 % after 5 reaction cycles. The decay of mineralization efficiency is probably ascribed to the adsorption of degradation intermediates on active sites of catalyst. The used catalyst retained over 96 % of its pristine reactivity after the thermal treatment (annealed ZFC-20 % at 600°C under Ar atmosphere for 2 h), indicating that the catalytic activity of ZFC-20 % could be partly recovered by simple thermal treatment. The FTIR spectra of catalysts were detected to verify the function groups on the surface of ZFC-20 % (the fresh, used and re-calcined catalysts). As shown in Fig. S9a, the peak of C–H at

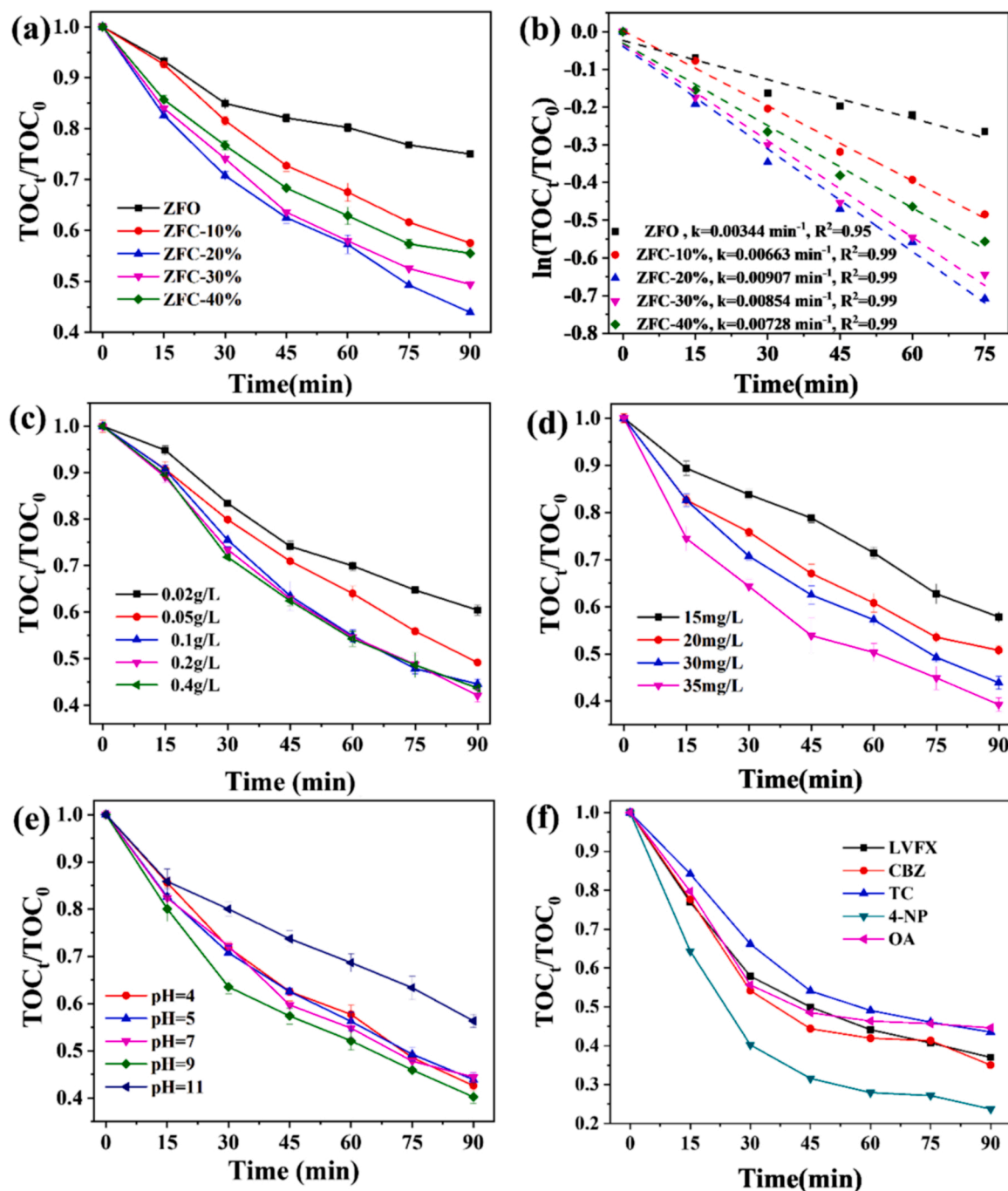


Fig. 3. (a) Mineralization of IBU with different Co dopant in catalytic ozonation system, (b) their correspondent pseudo-first-order kinetic curves; Effect of (c) catalysts dosage, (d) ozone concentration and (e) initial pH on catalytic activity; (f) Mineralization of different pollution in ZFC-20 %/ O_3 system. (Conditions: [ZFC-20 %] = 0.2 g/L, O_3 = 30 mg/L, [IBU] = 20 mg/L, [LVFX] = [CBZ] = [TC] = [4-NP] = 20 mg/L, [OA] = 50 mg/L).

2960.27 cm^{-1} was enhanced after degradation of IBU [27,28], which might be assigned to intermediates of IBU adsorbed on the surface of ZFC-20 %. Then it disappeared after re-calcination, implying the intermediates were decomposed. Besides, the concentration of leached iron and cobalt was examined during the cycling runs, which was less than 0.015 mg/L and 0.138 mg/L after each cycling (Fig. S9b). Furthermore, as presented in Fig. S9(c-d), the XRD patterns and Raman spectra of used catalyst displayed that there was no apparent difference between the used and fresh sample, implying that ZFC-20 % exhibited excellent stability during reaction.

3.3. Exploration of catalytic ozonation process

3.3.1. Discerning activated oxygen species for IBU degradation

Para-chlorobenzoic acid (p-CBA) could act as $\cdot OH$ probe to react rapidly with $\cdot OH$ ($k_{p\text{-CBA}/\cdot OH} = 5 \times 10^9\text{ M}^{-1}\text{s}^{-1}$) and shows poor reactivity with ozone ($k_{p\text{-CBA}/O_3} \leq 0.15\text{ M}^{-1}\text{s}^{-1}$). The decreasing concentration of p-CBA signified the indirect measure of $\cdot OH$ production. As shown in Fig. S10a, ZFO/ O_3 and ZFC-20 %/ O_3 systems obtained higher reaction rate than sole ozone, suggesting that ZFO and ZFC-20 % promote the generation of $\cdot OH$. The ZFC-20 % catalyst displayed similar p-CBA consumption with ZFO, implying that they had approximate $\cdot OH$ production. Besides, the $\cdot OH$ was further detected using fluorescence

spectroscopy by adding 0.65 mM terephthalic acid (TA) as the probe compound, which can trap $\cdot\text{OH}$ radicals to form highly fluorescent 2-hydroxyterephthalic acid (2-HTA) [29]. The concentration of 2-HTA was directly proportional to the amount of $\cdot\text{OH}$, which was determined by the fluorescent signals at the excitation wavelength of 315 nm. As presented in Fig. S10b, in comparison with ZFO, ZFC-20 % showed slightly lower signal intensity at 425 nm, indicating that introduction of Co component did not further improve the generation of $\cdot\text{OH}$. It can be concluded that the Fe sites might serve as the $\cdot\text{OH}$ producers rather than Co sites. Compared with fresh ZFC-20 %, the Fe(II)/Fe(III) in XPS spectra of used catalyst declined from 0.82 to 0.74 (Fig. S11), suggesting that Fe (II) was oxidized to Fe(III) by ozone. It implied that electrons were transferred from surface Fe(II), suggesting that iron species took part in the redox reaction of ozone decomposition for $\cdot\text{OH}$ generation.

Moreover, in-situ EPR is an effective technique to identify the generated activated oxygen species. The reagent of 5,5-dimethyl-1-pyrroline N-oxide (DMPO) acted as an effective spin trapping agent to probe reactive radicals. As shown in Fig. 4a, the typical four-fold peaks with an intensity ratio of 1:2:2:1 ($\alpha_N = 14.87$ G $\alpha_H = 14.87$ G) were assigned to DMPO- $\cdot\text{OH}$ adduct in sole ozonation and catalytic ozonation system. It can be observed that the signal of DMPO- $\cdot\text{OH}$ in ZFC-20 %/ O_3 was slightly weaker than that in ZFO/ O_3 process, suggesting that the generation of $\cdot\text{OH}$ was not facilitated with the introduction of Co. These results were consistent with the fluorescence spectroscopy measurements above. The EPR signals of DMPO- $\text{O}_2^{\cdot-}$ adducts were not observed in sole ozonation and catalytic ozonation system (Fig. S12a), revealing that the $\text{O}_2^{\cdot-}$ was not generated in all the process. Additionally, TEMP was employed as spin trapping agent to capture $^1\text{O}_2$. As illustrated in

Fig. S12b, the system of O_3 , ZFO/ O_3 and ZFC-20 %/ O_3 exhibited almost the same intensity of peaks with background signal, implying that $^1\text{O}_2$ may not be involved in catalytic ozonation system.

The radical scavenging tests were explored to clarify the catalytic mechanism. In order to evaluate the contribution of $\cdot\text{OH}$ to the mineralization of IBU in ZFC-20 %/ O_3 process, bicarbonate was added to scavenge $\cdot\text{OH}$. The reaction rate of bicarbonate with $\cdot\text{OH}$ ($k = 8.5 \times 10^6 \text{ M}^{-1}\text{s}^{-1}$) is much higher than that with ozone ($k < 0.1 \text{ M}^{-1}\text{s}^{-1}$) [30]. As illustrated in Fig. 4b, bicarbonate quencher caused negligible suppression to the mineralization of IBU in ZFC-20 %/ O_3 system, suggesting that $\cdot\text{OH}$ was not the major ROS for IBU mineralization during ZFC-20 % catalytic ozonation. Furthermore, the contribution of $\cdot\text{OH}$ for IBU removal was also explored by quenching test. *Tert*-butanol (TBA) was chosen as the quencher of $\cdot\text{OH}$, which was inert with ozone molecules ($k_{\text{TBA}/\text{O}_3} = 3 \times 10^{-5} \text{ M}^{-1}\text{s}^{-1}$). The added TBA (5 mM) was enough to scavenge the produced $\cdot\text{OH}$ because p-CBA removal was completely suppressed with the presence of TBA in ZFC-20 %/ O_3 system (Fig. S10c). As shown in Fig. 4d, when TBA was added, the IBU degradation efficiency slightly decreased from 89 % to 76 % in ZFC-20 % catalytic ozonation. The slight suppression of IBU removal suggested that $\cdot\text{OH}$ participated the reaction but it was not the dominant oxidation species. The excellent activity performance in ZFC-20 %/ O_3 system might result from other activated oxygen species. The in-situ Raman spectroscopy was used to determine intermediated oxygen species generated on catalysts (Fig. 4c). Different from ZFO, a weak Raman peak occurred at 936.16 cm^{-1} upon ozone addition in ZFC-20 % suspension, assigned to surface atomic oxygen species $^*\text{O}$ with the presence of Vo [10,11]. The peak disappeared with the addition of IBU, implying that $^*\text{O}$ might be

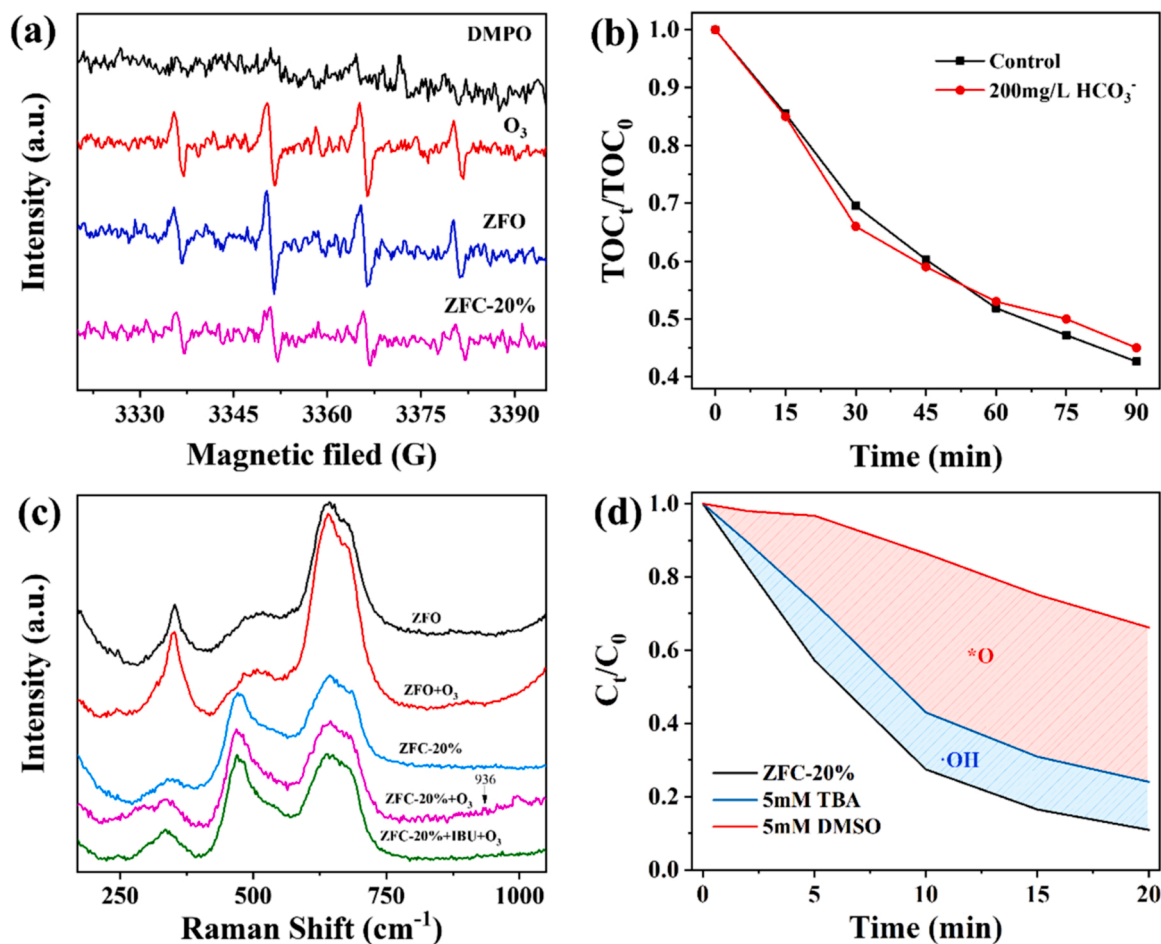


Fig. 4. (a) EPR spectra of DMPO- $\cdot\text{OH}$; (b) Effect of bicarbonate on catalytic performance of ZFC-20 %/ O_3 system; (c) In-situ Raman spectra of ZFO and ZFC-20 %; (d) Quenching tests of active species during the degradation of IBU in the ZFC-20 %/ O_3 process.

responsible for IBU degradation in ZFC-20 %/ O_3 process. Dimethyl sulfoxide (DMSO, $k_{DMSO/O_3} = 0.42 \text{ M}^{-1}\text{s}^{-1}$) can scavenge both of $\cdot O$ and $\cdot OH$ [7], which was selected as the quencher to evaluate the contribution of $\cdot O$ in IBU removal. Notably, the IBU removal drastically decreased from 89 % to 34 % with the appearance of DMSO. The inhibition of IBU degradation with DMSO was much obvious than that with TBA, signifying that $\cdot O$ played a major role in ZFC-20 %/ O_3 process rather than $\cdot OH$. Taken together, the above results from experiments implied that both of the $\cdot O$ and $\cdot OH$ participated the pollutants removal, while nonradical oxidation pathway with $\cdot O$ dominated the ZFC-20 %/ O_3 catalysis for IBU removal.

In order to determine the oxidation pathway dominated by different ROS, the degradation intermediates of IBU in ZFO/ O_3 and ZFC-20 %/ O_3 system were investigated by LC-MS in ESI positive and negative ion scan model. The chemical details of intermediates were presented in Table S3-S4 and Fig. S13. The intermediates variation during different degradation process were shown in Fig. 5(a-b). Based on the analysis of intermediates, three degradation pathways were proposed in Scheme 1. For path I, IBU was converted to P1 ($M = 220$) through hydroxylation and deprotonation with the attack of $\cdot OH$, which was further oxidized to product P2 ($M = 194$) [31]. The concentration of P1 in ZFO was much higher than ZFC-20 %, suggesting that path I was the main degradation process in ZFO/ O_3 system. For path II, P3 ($M = 178$) was produced by the attack of the $\cdot OH$ towards propionic acid of IBU through hydroxylation and decarboxylation [31,32]. Subsequently, P3 was oxidized to generate P4 and the product of P8 was formed with the cleavage of isobutyl moiety of P4 though the oxidation of $\cdot OH$ and $\cdot O$. For path III, intermediate P6 was obtained by the decarboxylation and dehydration reaction and the P7 conversion process might be formed by addition reaction by radical and $\cdot O$. The product P7 can also be transformed to P8 by the attack of $\cdot O$. As shown in Fig. 5, the product P7 increased during the ZFO/ O_3 process, while it increased first and then declined in ZFC-20 %/ O_3 system. Compared with ZFO, the concentration of generated P8 in ZFC-20 % was much higher, suggesting that $\cdot O$ was favorable for the transformation of P7 to P8. Generally, the transformation products were further oxidized to form chain organic acid. The products of chain organic acids (such as P5, P9, P10 and so on) were accumulated in the ZFO/ O_3 . Expectantly, those organic acids were further degraded completely in ZFC-20 %/ O_3 system. In general, the IBU degradation in ZFO and ZFC-20 % catalysis followed diverse pathway with different oxidant species. The degradation path I and II played more important role in the ZFO/ O_3 process with the $\cdot OH$ attack. Differently, the IBU degradation pathway mainly follows path II and III with the dominant participation of $\cdot O$ in ZFC-20 % catalysis.

3.3.2. Role of oxygen vacancy

The O1s XPS spectra of as-prepared catalysts were investigated in Fig. 6a. The peak at 531.3 eV was corresponded to surface oxygen species adsorbed on Vo (O_{ads}). The content of O_{ads} in catalysts follows the order of ZFC-20 % > ZFC-30 % > ZFC-40 % > ZFC-10 %, which was in

accordance with Vo concentration. As displayed in Fig. 6b, it can be observed that the mineralization rate constant was consistent with the variation of Vo, suggesting that Vo might be responsible for IBU degradation. Besides, solid-EPR was performed to analyze the Vo in catalysts. As shown in Fig. 6c, asymmetric EPR signals at $g = 2.000$ were observed upon the addition of catalysts, which arose from the unpaired electrons on Vo. The strong EPR signal in ZFC confirms that the substitution of Co species leads to increased amount of Vo [33]. The sequence of Vo concentration was also in consistent with the mineralization rate constant, which further suggested that Vo played an important role in catalysis. In addition, the Vo was also introduced on the surface of ZFO with hydrogenation treatment (ZFO-H, Fig. S14a), which significantly improved the mineralization for IBU (Fig. S14b). It further suggested that Vo might be responsible for the enhancement of catalytic performance. According to previous reports, Vo could behave as surface Lewis-acid sites [34], which was favorable for the chemical bonding with ozone. Generally, Lewis-acid sites can be covered by a strong Lewis base such as phosphate [35,36]. As illustrated in Fig. S14c, the introduction of phosphate had ignorable effect on IBU mineralization in the process of sole ozonation. However, catalytic performance of ZFC-20 % was significantly hindered with the presence of phosphate because the active sites of Vo were shielded by phosphate, implying the important role of Vo for catalysis. Additionally, the XPS spectra of Co2p for the fresh and used ZFC-2 % showed similar proportion of Co(III)/Co(II) and located at same binding energy (Fig. S15), suggesting that Co sites might not be the decisive species for the improved activity in ZFC-20 %/ O_3 process.

The formation of Vo can be confirmed by H_2 -TPR with investigation of the reducibility of surface oxygen species. In comparison with ZFO (Fig. S16a), the peak at 339.5 °C was much stronger in ZFC-20 %, corresponding to the reduction of surface-adsorbed oxygen species on Vo [18]. The result suggested the generation of Vo on ZFC-20 % with the substitution of Co species. Furthermore, O_2 -TPD could be used to quantify Vo and lattice oxygen to some extent [29]. The oxygen desorption peak around lower temperature region (around 100–400 °C) corresponded to weakly chemisorbed oxygen on Vo, while the rest peaks at higher temperature ranges were assigned to lattice oxygen evolved from catalyst [37]. Compared with ZFO, the peak arising from Vo in ZFC-20 % showed much higher area (Fig. S16b), suggesting that more Vo was generated on ZFC-20 %. In addition, the rough surface in HRTEM images of ZFC-20 % highlighted the lattice distortion and flabby weakening of lattice oxygen bonds (Fig. S16c), implying the introduction of Vo.

3.3.3. Mechanism discussion

DFT calculations (details in Text S5) were carried out to gain insight into the role of Vo in the catalytic ozonation system. The favorable adsorption behavior of O_3 on different sites of models ZFO and ZFC (with Vo) was shown in Fig. 7. The adsorption energy of O_3 at different four sites (Fe site on ZFO, Vo site on ZFC-20 %, Co site adjacent to Vo on ZFC-

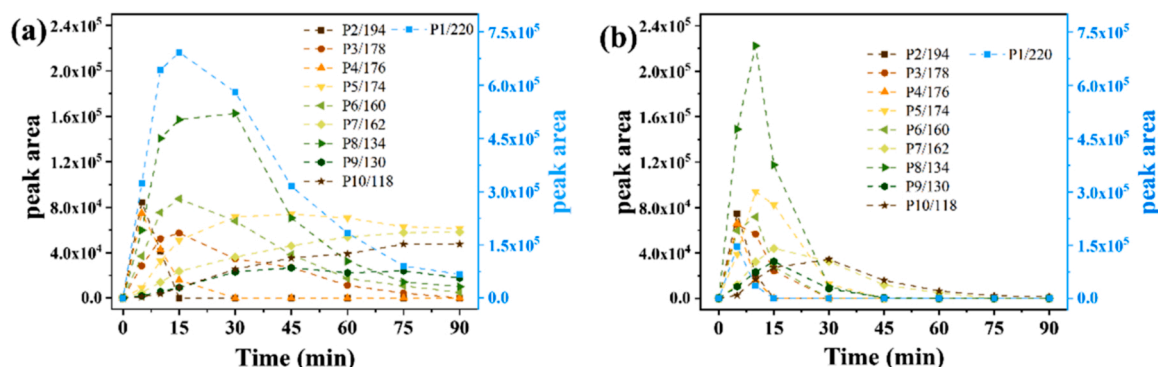
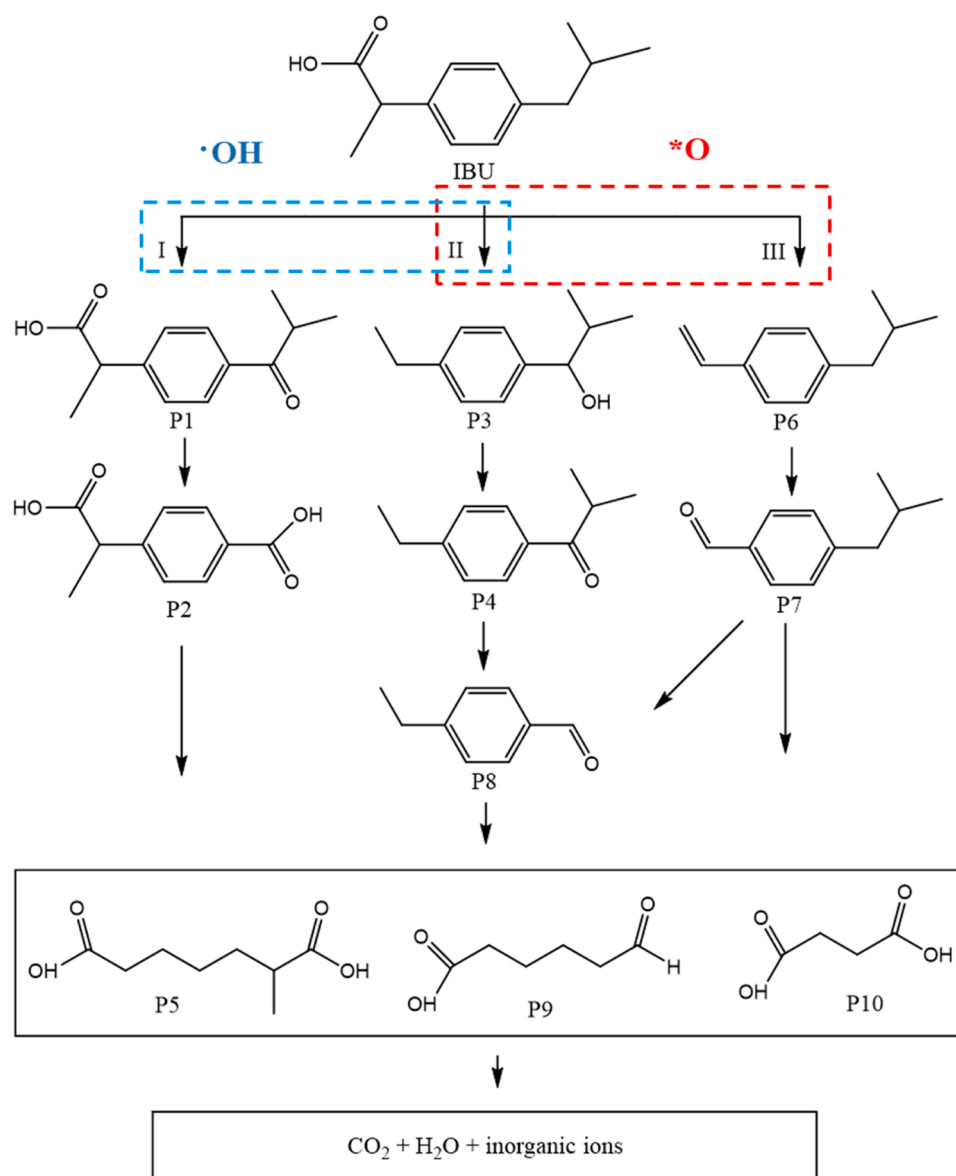


Fig. 5. Evolution of major intermediates of IBU in (a) ZFO/ O_3 system and (b) ZFC-20 %/ O_3 process.



Scheme 1. Proposed IBU degradation pathways.

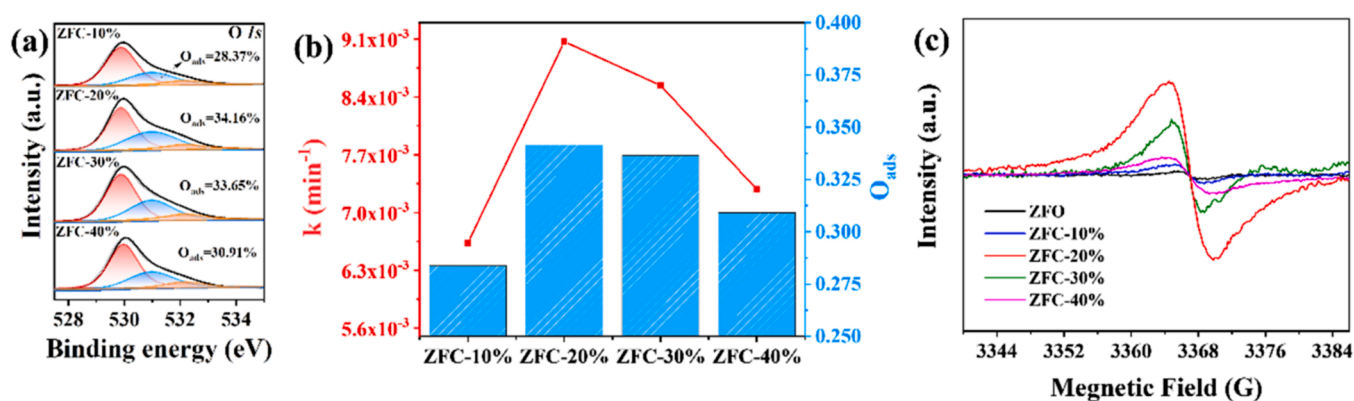


Fig. 6. (a) XPS high-resolution of O 1s in ZFC; (b) Relationships between the oxygen vacancy content and kinetic constants in catalytic ozonation; (c) Solid low-temperature (90 K) EPR spectra of catalysts.

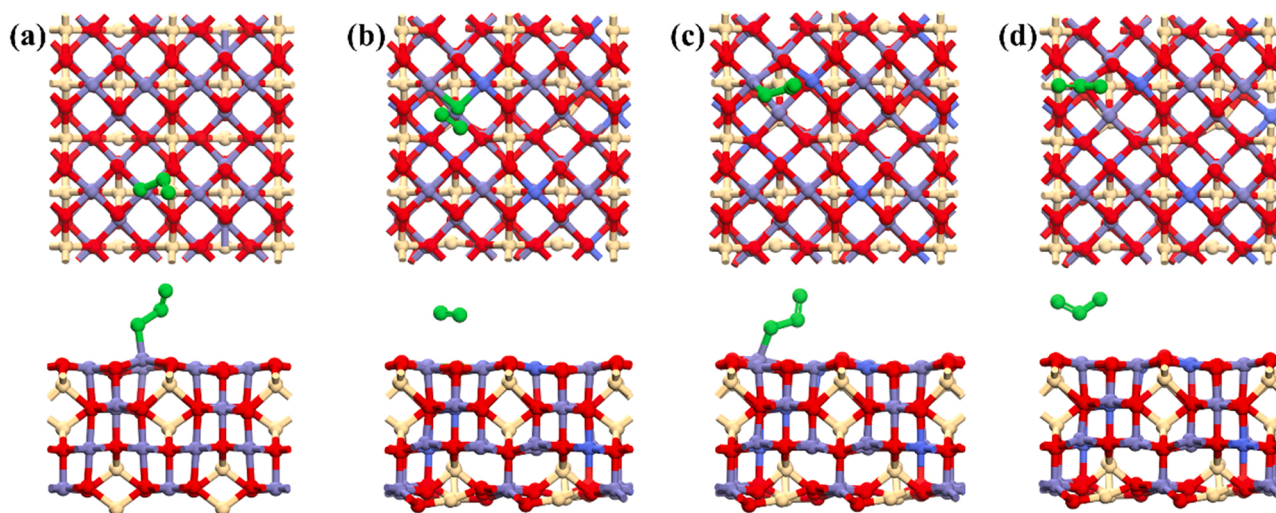
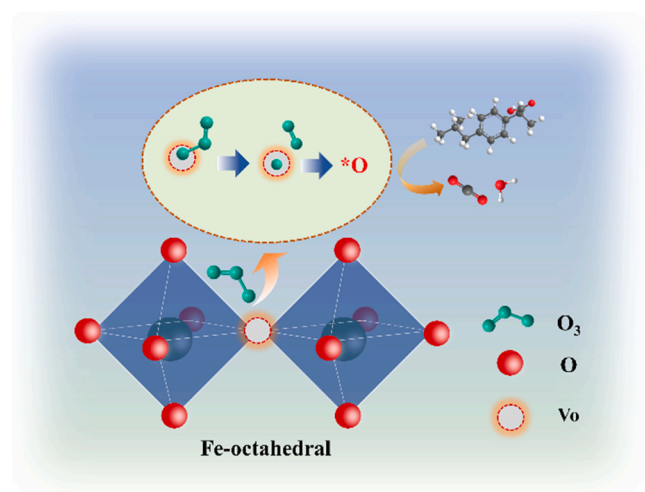


Fig. 7. DFT models of the favorable adsorption structure for ozone molecule on the site of: (a) Fe site on ZFO, (b) Vo on ZFC-20 %, (c) Co site adjacent to Vo on ZFC-20 %, (d) Fe site adjacent to Vo on ZFC-20 %.

20 %, Fe site adjacent Vo to on ZFC-20 %) in models were calculated. As shown in Table S5, the O₃ molecules adsorption energy of Vo site was calculated to be -3.38 eV, which is more negative than that of other sites. In other word, Vo on ZFC-20 % possessed the highest potentiality, indicating the strong affinity with O₃ molecule. The O-O bond in ozone can be spontaneously dissociated at Vo, triggering the formation of surface-bounded atomic oxygen *O and a free dioxygen molecule (Fig. 7b). The *O produced at active sites of Vo could induce a non-radical oxidation pathway on the surface of ZFC-20 %. Therefore, DFT calculation indicated that the Vo was the active sites for the generation of *O during the catalytic ozonation.

Based on above analysis, the ozonation mechanism of the ZFC-20 %/O₃ process was proposed in Scheme 2. Compared with ZFO, new reactive sites of Vo were introduced on the surface of ZFC-20 % with Co doping. During the catalytic ozonation process, the ozone was firstly adsorbed on Vo. Then, the O-O in ozone was spontaneously dissociated in Vo, triggering the formation of atomic oxygen *O and a free dioxygen molecule. Finally, the surface adsorbed *O can react with the organic pollutants.



Scheme 2. Proposed mechanism of catalytic ozonation on ZFC-20 % with enriched Vo.

3.4. Catalytic ozonation performance in real wastewater treatment

Inorganic anions are ubiquitous in actual wastewaters and can pose inhibition effect on pollutants removal in traditional radical-based oxidation process because of its radical-scavenging character [38,39]. As reported in several literatures, nonradical-based oxidation process could resist coexisting ions, which might relieve the inhibition effect [40,41]. Hence, the effect of common anions (Cl⁻, SO₄²⁻, NO₃⁻) on catalytic performance in nonradical-based system were investigated in ZFC-20 %/O₃ system. As displayed in Fig. 8, the mineralization of IBU was examined in ZFC-20 %/O₃ process with different concentration of anions (20–200 mM Cl⁻, SO₄²⁻, NO₃⁻). As for Cl⁻, low concentration (20 mM) of chloride showed negligible effect on IBU mineralization. When chloride concentration increased even to 100 or 200 mM, the TOC removal efficiency only reduced 10 %, which showed much lower inhibition than that in radical-based oxidation process [38,42]. As for SO₄²⁻, the TOC removal reduced from 59 % to 55–57 % with sulfate ion concentration range from 20 to 200 mM within 120 min, suggesting the sulfate ion showed negligible effect on IBU removal in ZFC-20 %/O₃ process. With the analogous orderliness, NO₃⁻ showed no noticeable effect on mineralization efficiency even under high salinity conditions (100 or 200 mM) with 7 % decrease of TOC value. Overall, the coexisting anions had a slight effect on IBU mineralization even at high concentration, suggesting that ZFC-20 %/O₃ system underwent less interference from common background anions in wastewater.

The treatment of coke-plant secondary effluent was investigated to further assess the catalytic performance of ZFC-20 %/O₃ under practical condition. The parameters of the practical wastewater were given in Table S6. The initial COD value of actual secondary effluent was 117 mg/L. After 180 min reaction (Fig. S17), the residual COD reached 47 mg/L in ZFC-20 %/O₃ process, which was below the emission limit of Chinese National Standard for the Wastewater Discharge (GB 18918-2002, 50 mg/L). The results suggested that ZFC-20 %/O₃ system had an application potential for real wastewater treatment.

4. Conclusion

The surface Vo-rich catalysts by lattice-doping Co into zinc ferrite spinel was successfully prepared through sol-gel method. The catalyst with abundant Vo exhibited effective oxidation of refractory organic pollutants during the catalytic ozonation process. The nonradical species of *O played major role in pollutants removal. Experiments and DFT calculation results revealed that Vo was the main active sites for the

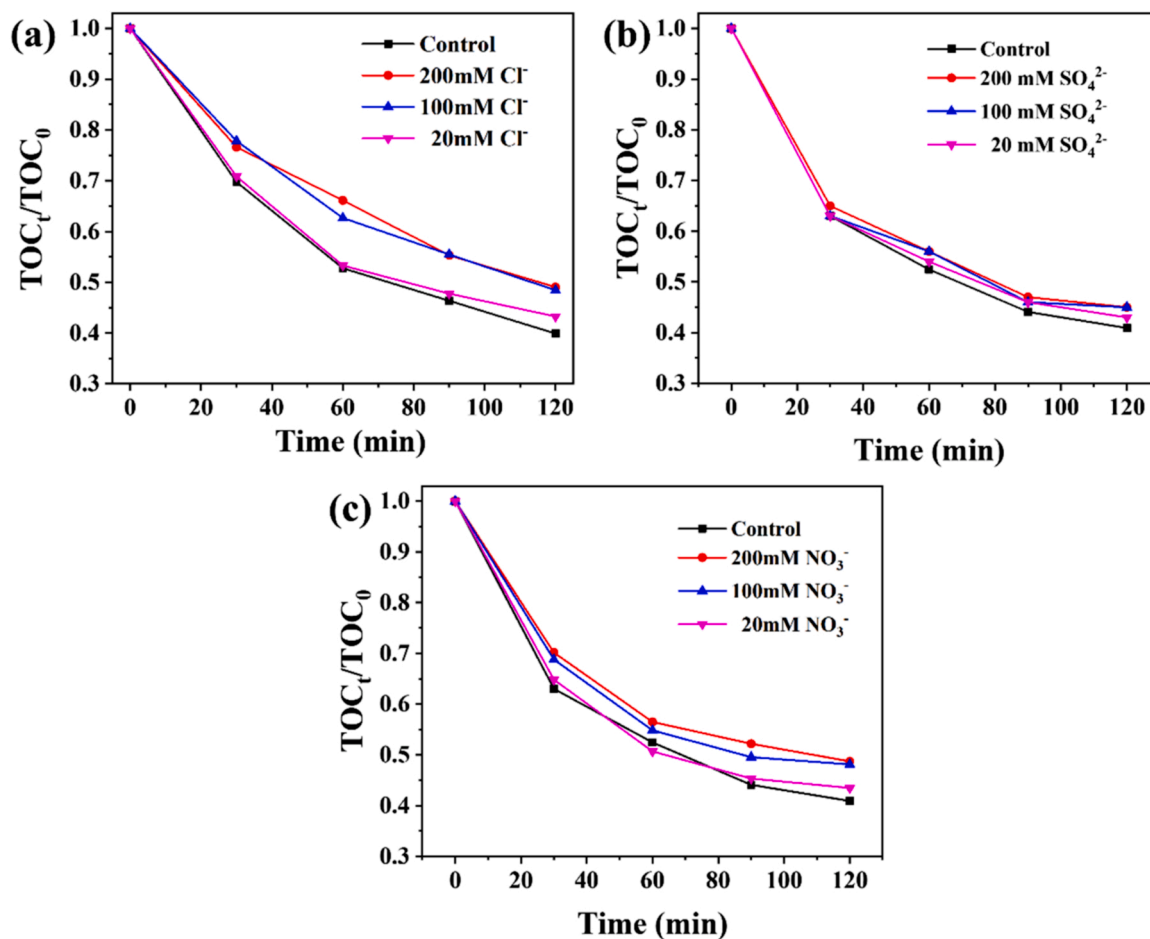


Fig. 8. Effect of the coexisting anions (a) Cl⁻, (b) SO₄²⁻ and (c) NO₃⁻. (Conditions: [ZFC-20 %] = 0.2 g/L, [IBU] = 20 mg/L, O₃ = 30 mg/L).

adsorption of ozone and generation of [•]O. The O-O in ozone was dissociated at Vo, triggering the formation of surface atomic oxygen [•]O. Additionally, the Vo-driven nonradical catalysis showed high resistance to the coexisting ions (200 mM Cl⁻, NO₃⁻ and SO₄²⁻) and exhibited excellent performance for actual wastewater treatment. This work provides an insight into regulation strategy of the oxidation pathways in catalytic ozonation process for efficient mineralization of refractory organic contaminants in complicated water matrices.

CRediT authorship contribution statement

Lanlan Liang: Investigation, Methodology, Data curation, Formal analysis, Writing – original draft. **Peike Cao:** Investigation, Writing – review & editing. **Xin Qin:** Conceptualization, Methodology. **Shuai Wu:** Investigation, Supervision. **Haokun Bai:** Supervision, Resources, Methodology. **Shuo Chen:** Investigation, Supervision. **Hongtao Yu:** Resources, Methodology. **Yan Su:** Conceptualization, DFT calculation. **Xie Quan:** Project administration, Supervision, Writing – review & editing, Funding acquisition.

Declaration of Competing Interest

The authors declare that they have no known competing financial interests or personal relationships that could have appeared to influence the work reported in this paper.

Data Availability

Data will be made available on request.

Acknowledgements

This work was supported by the National Natural Science Foundation of China (no. 21936002) and National Key Research and Development Program of China (2020YFA0211001).

Appendix A. Supporting information

Supplementary data associated with this article can be found in the online version at [doi:10.1016/j.apcatb.2022.122321](https://doi.org/10.1016/j.apcatb.2022.122321).

References

- [1] J. Wu, L. Ma, Y. Chen, Y. Cheng, Y. Liu, X. Zha, Catalytic ozonation of organic pollutants from bio-treated dyeing and finishing wastewater using recycled waste iron shavings as a catalyst: removal and pathways, *Water Res.* 92 (2016) 140–148.
- [2] C. Ouyang, K. Wei, X. Huang, M. Gamal El-Din, X. Zhang, Bifunctional Fe for induced graphitization and catalytic ozonation based on a Fe/N-doped carbon-Al₂O₃ framework: theoretical calculations guided catalyst design and optimization, *Environ. Sci. Technol.* 55 (2021) 11236–11244.
- [3] Y. Yuan, G. Xing, S. Garg, J. Ma, X. Kong, P. Dai, T.D. Waite, Mechanistic insights into the catalytic ozonation process using iron oxide-impregnated activated carbon, *Water Res.* 177 (2020), 115785.
- [4] K. Wei, X. Cao, W. Gu, P. Liang, X. Huang, X. Zhang, Ni-induced C-Al₂O₃-framework (NiCAF) supported core-multishell catalysts for efficient catalytic ozonation: a structure-to-performance study, *Environ. Sci. Technol.* 53 (2019) 6917–6926.
- [5] J. Bing, C. Hu, Y. Nie, M. Yang, J. Qu, Mechanism of catalytic ozonation in Fe₂O₃/Al₂O₃@SBA-15 aqueous suspension for destruction of ibuprofen, *Environ. Sci. Technol.* 49 (2015) 1690–1697.
- [6] R. Luo, M. Li, C. Wang, M. Zhang, M.A. Nasir Khan, X. Sun, J. Shen, W. Han, L. Wang, J. Li, Singlet oxygen-dominated non-radical oxidation process for efficient degradation of bisphenol A under high salinity condition, *Water Res.* 148 (2019) 416–424.

- [7] G. Yu, Y. Wang, H. Cao, H. Zhao, Y. Xie, Reactive oxygen species and catalytic active sites in heterogeneous catalytic ozonation for water purification, *Environ. Sci. Technol.* 54 (2020) 5931–5946.
- [8] Y. Wang, X. Duan, Y. Xie, H. Sun, S. Wang, Nanocarbon-based catalytic ozonation for aqueous oxidation: engineering defects for active sites and tunable reaction pathways, *ACS Catal.* 10 (2020) 13383–13414.
- [9] Y. Wang, J. Xi, X. Duan, W. Lv, H. Cao, C. Chen, Z. Guo, Y. Xie, S. Wang, The duet of surface and radical-based carbocatalysis for oxidative destructions of aqueous contaminants over built-in nanotubes of graphite, *J. Hazard. Mater.* 384 (2020), 121486.
- [10] J. Bing, C. Hu, L. Zhang, Enhanced mineralization of pharmaceuticals by surface oxidation over mesoporous γ -Ti-Al₂O₃ suspension with ozone, *Appl. Catal. B: Environ.* 202 (2017) 118–126.
- [11] T. Zhang, W. Li, J.P. Croue, Catalytic ozonation of oxalate with a cerium supported palladium oxide: an efficient degradation not relying on hydroxyl radical oxidation, *Environ. Sci. Technol.* 45 (2011) 9339–9346.
- [12] R. Ding, W. Li, C. He, Y. Wang, X. Liu, G. Zhou, Y. Mu, Oxygen vacancy on hollow sphere CuFe₂O₄ as an efficient Fenton-like catalysis for organic pollutant degradation over a wide pH range, *Appl. Catal. B: Environ.* 291 (2021), 120069.
- [13] Y. Bu, H. Li, W. Yu, Y. Pan, L. Li, Y. Wang, L. Pu, J. Ding, G. Gao, B. Pan, Peroxydisulfate activation and singlet oxygen generation by oxygen vacancy for degradation of contaminants, *Environ. Sci. Technol.* 55 (2021) 2110–2120.
- [14] L. Liu, Q. Liu, Y. Wang, J. Huang, W. Wang, L. Duan, X. Yang, X. Yu, X. Han, N. Liu, Nonradical activation of peroxydisulfate promoted by oxygen vacancy-laden NiO for catalytic phenol oxidative polymerization, *Appl. Catal. B: Environ.* 254 (2019) 166–173.
- [15] G. Zhai, S. Liu, S. Si, Y. Liu, H. Zhang, Y. Mao, M. Zhang, Z. Wang, H. Cheng, P. Wang, Z. Zheng, Y. Dai, B. Huang, Oxygen vacancies enhanced ozonation toward phenol derivatives removal over Ov-Bi₂O₃, *ACS EST Water* 2 (2022) 1725–1733.
- [16] A.A. Esmailpour, J. Horlyck, P. Kumar, C. Tsounis, J. Yun, R. Amal, J. Scott, Engineering multidefects on Ce₃Si_{1-x}O₂₋₈ nanocomposites for the catalytic ozonation reaction, *Small* 18 (2022), 2103530.
- [17] Y. Wang, L. Chen, H. Cao, Z. Chi, C. Chen, X. Duan, Y. Xie, F. Qi, W. Song, J. Liu, S. Wang, Role of oxygen vacancies and Mn sites in hierarchical Mn₂O₃/LaMnO₃₋₈ perovskite composites for aqueous organic pollutants decontamination, *Appl. Catal. B: Environ.* 245 (2019) 546–554.
- [18] H. Zhang, C. Li, L. Lyu, C. Hu, Surface oxygen vacancy inducing peroxymonosulfate activation through electron donation of pollutants over cobalt-zinc ferrite for water purification, *Appl. Catal. B: Environ.* 270 (2020), 118874.
- [19] Y. Gao, W. Zhu, J. Liu, P. Lin, J. Zhang, T. Huang, K. Liu, Mesoporous sulfur-doped CoFe₂O₄ as a new Fenton catalyst for the highly efficient pollutants removal, *Appl. Catal. B: Environ.* 295 (2021), 120273.
- [20] B. Zhang, L. Wang, Y. Zhang, Y. Ding, Y. Bi, Ultrathin FeOOH nanolayers with abundant oxygen vacancies on BiVO₄ photoanodes for efficient water oxidation, *Angew. Chem. Int. Ed.* 57 (2018) 2248–2252.
- [21] W. Wang, Y. Liu, Y. Yue, H. Wang, G. Cheng, C. Gao, C. Chen, Y. Ai, Z. Chen, X. Wang, The confined interlayer growth of ultrathin two-dimensional Fe₃O₄ nanosheets with enriched oxygen vacancies for peroxymonosulfate activation, *ACS Catal.* 11 (2021) 11256–11265.
- [22] H. Zhu, M. Fang, Z. Huang, Y. Liu, K. Chen, C. Tang, M. Wang, L. Zhang, X. Wu, Novel carbon-incorporated porous ZnFe₂O₄ nanospheres for enhanced photocatalytic hydrogen generation under visible light irradiation, *RSC Adv.* 6 (2016) 56069–56076.
- [23] S. Majumder, N.D. Quang, T.T. Hien, N.D. Chinh, N.M. Hung, H. Yang, C. Kim, D. Kim, Effect of SILAR-anchored ZnFe₂O₄ on the BiVO₄ nanostructure: an attempt towards enhancing photoelectrochemical water splitting, *Appl. Surf. Sci.* 546 (2021), 149033.
- [24] S. Afzal, X. Quan, J. Zhang, High surface area mesoporous nanocast LaMO₃ (M = Mn, Fe) perovskites for efficient catalytic ozonation and an insight into probable catalytic mechanism, *Appl. Catal. B: Environ.* 206 (2017) 692–703.
- [25] P. Yan, J. Shen, Y. Zhou, L. Yuan, J. Kang, S. Wang, Z. Chen, Interface mechanism of catalytic ozonation in an α -Fe_{0.9}Mn_{0.1}OOH aqueous suspension for the removal of iohexol, *Appl. Catal. B: Environ.* 277 (2020), 119055.
- [26] D. Yuvali, I. Narin, M. Soylak, E. Yilmaz, Green synthesis of magnetic carbon nanodot/graphene oxide hybrid material (Fe₃O₄@C-nanodot@GO) for magnetic solid phase extraction of ibuprofen in human blood samples prior to HPLC-DAD determination, *J. Pharm. Biomed.* 179 (2020), 113001.
- [27] S. Mallick, S. Pattnaik, K. Swain, P.K. De, A. Saha, G. Ghoshal, A. Mondal, Formation of physically stable amorphous phase of ibuprofen by solid state milling with kaolin, *Eur. J. Pharm. Biopharm.* 68 (2008) 346–351.
- [28] M. Grochowicz, A. Kierys, TG/DSC/FTIR studies on the oxidative decomposition of polymer-silica composites loaded with sodium ibuprofen, *Polym. Degrad. Stabil.* 138 (2017) 151–160.
- [29] S. Afzal, X. Quan, S. Lu, Catalytic performance and an insight into the mechanism of CeO₂ nanocrystals with different exposed facets in catalytic ozonation of p-nitrophenol, *Appl. Catal. B: Environ.* 248 (2019) 526–537.
- [30] J. Wang, X. Quan, S. Chen, H. Yu, G. Liu, Enhanced catalytic ozonation by highly dispersed CeO₂ on carbon nanotubes for mineralization of organic pollutants, *J. Hazard. Mater.* 368 (2019) 621–629.
- [31] B. Zhang, Q. Wang, Y. Zhang, Y. Teng, M. Fan, Degradation of ibuprofen in the carbon dots/Fe₃O₄@carbon sphere pomegranate-like composites activated persulfate system, *Sep. Purif. Technol.* 242 (2020), 116820.
- [32] Y. Zhang, B. Zhang, Y. Teng, J. Zhao, X. Sun, Heterogeneous activation of persulfate by carbon nanofiber supported Fe₃O₄@carbon composites for efficient ibuprofen degradation, *J. Hazard. Mater.* 401 (2021), 123428.
- [33] Y. Wang, F. Wang, Q. Song, Q. Xin, S. Xu, J. Xu, Heterogeneous ceria catalyst with water-tolerant Lewis acidic sites for one-pot synthesis of 1,3-diols via Prins condensation and hydrolysis reactions, *J. Am. Chem. Soc.* 135 (2013) 1506–1515.
- [34] A. Lv, C. Hu, Y. Nie, J. Qu, Catalytic ozonation of toxic pollutants over magnetic cobalt and manganese co-doped γ -Fe₂O₃, *Appl. Catal. B: Environ.* 100 (2010) 62–67.
- [35] Y. Wang, H. Cao, L. Chen, C. Chen, X. Duan, Y. Xie, W. Song, H. Sun, S. Wang, Tailored synthesis of active reduced graphene oxides from waste graphite: structural defects and pollutant-dependent reactive radicals in aqueous organics decontamination, *Appl. Catal. B: Environ.* 229 (2018) 71–80.
- [36] S. Guo, H. Wang, W. Yang, H. Fida, L. You, K. Zhou, Scalable synthesis of Ca-doped α -Fe₂O₃ with abundant oxygen vacancies for enhanced degradation of organic pollutants through peroxymonosulfate activation, *Appl. Catal. B: Environ.* 262 (2020), 118250.
- [37] J. Zhang, X. Weng, Z. Wu, Y. Liu, H. Wang, Facile synthesis of highly active LaCoO₃/MgO composite perovskite via simultaneous co-precipitation in supercritical water, *Appl. Catal. B: Environ.* 126 (2012) 231–238.
- [38] H. Zheng, J. Bao, Y. Huang, L. Xiang, Faheem, B. Ren, J. Du, M.N. Nadagouda, D. D. Dionysiou, Efficient degradation of atrazine with porous sulfurized Fe₂O₃ as catalyst for peroxymonosulfate activation, *Appl. Catal. B: Environ.* 259 (2019), 118056.
- [39] Y. Sun, R. Li, C. Song, H. Zhang, Y. Cheng, A. Nie, H. Li, D.D. Dionysiou, J. Qian, B. Pan, Origin of the improved reactivity of MoS₂ single crystal by confining lattice Fe atom in peroxymonosulfate-based Fenton-like reaction, *Appl. Catal. B: Environ.* 298 (2021), 120537.
- [40] Z. Guo, Y. Si, W. Xia, F. Wang, H. Liu, C. Yang, W. Zhang, W. Li, Electron delocalization triggers nonradical Fenton-like catalysis over spinel oxides, *Proc. Natl. Acad. Sci. USA* 119 (2022).
- [41] H. Li, C. Shan, B. Pan, Fe(III)-doped g-C₃N₄ mediated peroxymonosulfate activation for selective degradation of phenolic compounds via high-valent iron-oxo species, *Environ. Sci. Technol.* 52 (2018) 2197–2205.
- [42] Z. Wu, Y. Wang, Z. Xiong, Z. Ao, S. Pu, G. Yao, B. Lai, Core-shell magnetic Fe₃O₄@Zn/Co-ZIFs to activate peroxymonosulfate for highly efficient degradation of carbamazepine, *Appl. Catal. B: Environ.* 277 (2020), 119136.